Arteriosclerosis, Thrombosis, and Vascular Biology

BASIC SCIENCES

Ex Vivo Study Using Diffusion Tensor Imaging to Identify Biomarkers of Atherosclerotic Disease in Human Cadaveric Carotid Arteries

Brooke Tornifoglio[ID], Alan J. Stone, Christian Kerskens, Caitríona Lally[ID]

BACKGROUND: This study aims to address the potential of ex vivo diffusion tensor imaging to provide insight into the microstructural composition and morphological arrangement of aged human atherosclerotic carotid arteries.

METHODS: In this study, whole human carotid arteries were investigated both anatomically and by comparing healthy and diseased regions. Nonrigid image registration was used with unsupervised segmentation to investigate the influence of elastin, collagen, cell density, glycosaminoglycans, and calcium on diffusion tensor imaging derived metrics (fractional anisotropy and mean diffusivity). Early stage atherosclerotic features were also investigated in terms of microstructural components and diffusion tensor imaging metrics.

RESULTS: All vessels displayed a dramatic decrease in fractional anisotropy compared with healthy animal arterial tissue, while the mean diffusivity was sensitive to regions of advanced disease. Elastin content strongly correlated with both fractional anisotropy (r>0.7, $P<0.001$) and mean diffusivity (r>−0.79, $P<0.0002$), and the thickened intima was also distinguishable from arterial media by these metrics.

CONCLUSIONS: These different investigations point to the potential of diffusion tensor imaging to identify characteristics of arterial disease progression, at early and late-stage lesion development.

GRAPHIC ABSTRACT: A graphic abstract is available for this article.

Key Words: atherosclerosis ■ carotid artery ■ diffusion tensor imaging ■ microstructure ■ smooth muscle cells

Progression of atherosclerotic plaques is often silent but can lead to the acute event of thrombosis and stroke, with plaque rupture being the most common cause.[1] Plaque rupture most commonly occurs where the plaque cap is the thinnest, and the highest density of macrophages have infiltrated.[1,2] While changes in the mechanical environment may cause the physical rupture of the plaque,[3] microstructural changes are responsible for the thinning and vulnerability of the plaque cap.[1] Smooth muscle cells tend to be absent at the site of rupture on the cap,[4] and the decreased collagen content coupled with infiltrating macrophages, which secrete proteolytic enzymes, facilitate an inflamed microenvironment which weakens the tissue's integrity. It has previously been shown in atherosclerotic coronary arteries that inflammation collocates with areas of increased wall stress.[5] Both high stress[5] and high strain[6,7] have been linked with plaque rupture. Even before advanced atherosclerotic lesion formation, however, earlier microstructural changes have been associated with stroke risk.[8] For this reason, it is critical to identify early microstructural changes for diagnosis that might better capture the stage of disease rather than simply geometric features, such as the currently used metric of percent stenosis.[9–11]

Many studies have looked to *ex vivo* magnetic resonance imaging (MRI) to obtain high-resolution images of atherosclerotic microstructure. Multi-contrast MRI protocols, such as proton-density weighted-, T1-, T2-, and

---

Nonstandard Abbreviations and Acronyms

DTI	diffusion tensor imaging
FA	fractional anisotropy
MD	mean diffusivity
MRI	magnetic resonance imaging
PLM	polarized light microscopy
SMC	smooth muscle cell

Highlights

- Decreased fractional anisotropy seen in aged human carotid arteries highlights potential for assessing vessel integrity prior to atherosclerotic lesion development.
- Mean diffusivity showed a sensitivity to unspecific advanced regions of disease.
- Elastin content showed a strong correlation with fractional anisotropy and mean diffusivity when using unsupervised automatic segmentation regardless of clustering input.
- Early atherosclerotic features are distinguishable from the vessel wall by both fractional anisotropy and mean diffusivity.

diffusion weighted imaging have been implemented with a view to characterising plaque components. While some studies show the promise of using all these sequences in combination to characterise morphological regions,[12–14] other studies point to the sensitivity of individual MR contrasts to specific atherosclerotic morphologies.[13–18] Karmonik, et al. showed the promise of using multi-contrast MRI in conjunction with unsupervised segmentation to identify major plaque components such as lipid, calcifications, fibrotic tissue, thrombus, and normal vessel wall.[19] These morphologies are dictated by changes in microstructural components and their quantity and quality vary significantly throughout plaque progression.[20–22] Quantitative susceptibility mapping has been explored with respect to specific microstructural components in arterial tissue and shown to be sensitive to changes in elastin and collagen content[23] and also has demonstrated a strong correlation with erythrocytes[24] in carotid plaques. Diffusion tensor imaging (DTI) has shown a strong sensitivity to cell and elastin content in arterial tissue models[25] and has recently been used to identify altered microstructural organisation in tissue models[26,27] and plaque tissue[28] with a strong negative correlation found between fractional anisotropy (FA), the degree of anisotropic diffusion, in the common carotid with age.[29]

This study focuses solely on DTI with the aim to investigate aged human carotid arteries thoroughly. DTI-derived metrics signifying the overall diffusion (mean diffusivity [MD]) and the degree of anisotropic diffusion (FA) were used to gauge the feasibility of this imaging technique to identify disease-driven microstructural changes. Multiple analyses were carried out in order to both investigate bulk changes in these noninvasive metrics as well as microstructure and morphological specific changes. Healthy and diseased areas of the carotids were identified from nondiffusion weighted images and confirmed by histology. Additionally, histology slices of the common carotid were registered to MRI slices to facilitate unsupervised segmentation based on the FA and MD metrics. Registered histology was also used to manually segment identifiable atherosclerotic morphologies and investigate the DTI-derived metrics and microstructural components in these regions. Together, these different approaches aimed to establish whether microstructurally sensitive DTI metrics are potentially suitable biomarkers of atherosclerosis progression and if so, what microstructural changes are driving measurable changes in the metrics.
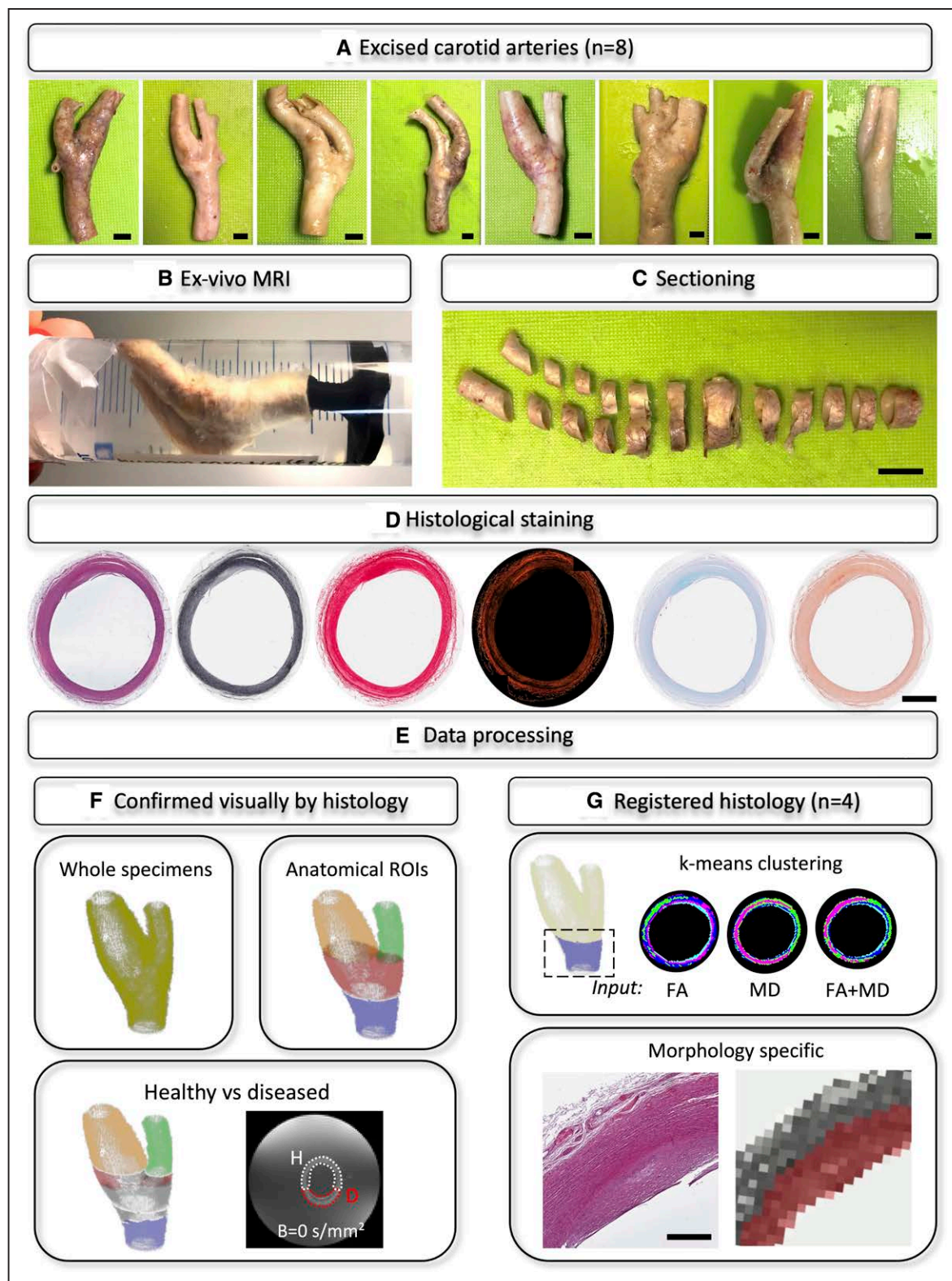
METHODS

An overview of the methods used in this study are shown in Figure 1. The data that support the findings of the study are available from the corresponding author upon reasonable request.

Human Carotid Arteries

Carotid arteries (n=8) were excised from 6 embalmed cadavers. Carotids were excised to include the common carotid, bifurcation, and both internal and external carotid arteries, see Figure 1A. All human cadaveric tissue was provided by The Royal College of Surgeons in Ireland and was used with approval from the Department of Anatomy, Royal College of Surgeons in Ireland institutional review board. Out of the 8 arteries from the 6 cadavers, 4 left carotids were excised from 4 different cadavers and the remaining 4 from 2 cadavers (both left and right carotids). The subjects (3 females and 3 males) ranged from 70 to 103 years in age (mean 78.25±11.2 years). Table 1 details the subjects used in this study. All 8 carotids were considered independent entities in this study as the focus was on identifying changes in arterial microstructure by DTI, not subject-specific trends. While the cause of death for all subjects was unrelated to cardiovascular disease, no additional information on risk factors, past medical history, or other cardiovascular diseases was available. The arteries were cleaned of connective tissue after excision and stored in phosphate-buffered saline (PBS) until imaging.

MR Imaging

The common carotid of the arteries was secured to a 3D printed holder, which was secured in a horizontal 50 ml falcon tube with fresh PBS for image acquisition, see Figure 1B. Due to the fixation of the carotids, their stiffness prevented any drooping or movement during scanning. Carotids were imaged individually in a small-bore horizontal 7 Tesla Bruker BioSpec 70/30 USR system. Details of the MR imaging performed can be found in Supplemental Material.[23,25,30–35] Of note are the 2

Figure 1. Brief overview of methods.
A, Excised cadaveric carotid arteries; scale bars are 5 mm. **B**, Example of carotid prior to ex vivo imaging, held in place by a 3D printed holder. **C**, Sectioning of a carotid for histological processing, 3 sections were taken for each subject; scale bar is 10 mm. **D**, Five histological stains were used for all carotids; left to right: Haematoxylin & Eosin, Verhoeff's elastin, Picrosirius red and polarized light microscopy of picrosirius red, Alcian blue, and Alizarin red. Scale bar is 2 mm. **E**, Magnetic resonance imaging data processing flow. **F**, Carotids were investigated as a whole, by anatomical region and by healthy (H) and diseased (D) regions non-specifically with histology visually used to confirm. **G**, Histology slices were registered to common carotids. K-means clustering with different inputs was investigated as well as specific morphological features. Scale bar is 0.5 mm.

Table 1. Details of the Cadaver Carotids Used in This Study

	Sex	Age	COD	Side	AHA classification
1	F	103	Aspiration pneumonia and Alzheimer	L	V
2	F	70	Chronic obstructive airway disease	L	IV and V
3	M	80	Pneumonia	R	VI
4	M	75	Metastatic prostate cancer	L	IV and V
5	F	80	Cerebellar syndrome	R	VI
6				L	V
7	M	69	Hospital acquired pneumonia	R	VI
8				L	VI

AHA classifications made based off morphological criteria.[65] AHA indicates American Heart Association; and COD, cause of death.

main DTI-derived metrics which are used in this study—FA and MD. The FA characterizes how diffusion in a voxel deviates from isotropic—signifying how anisotropic, or aligned in one predominant direction, the diffusion is.[36] The MD is the average of the 3 eigenvalues in the diffusion tensor and represents the average diffusion occurring in voxel, independent of orientation.[36] For example, in background PBS, you would expect a low FA value due to no preferred diffusion direction and a high MD value from isotropic diffusion in all directions. Tractography was also performed to visualize the tissue microstructure using the following parameters: seed point resolution and step size: 0.3125 μm, seed FA threshold: 0.075, tracking FA range: 0.075 to 1, fiber length: 1 to 50 mm, and angular threshold: 90°.

Histological Analysis

Histology Processing

For histological processing, 2 to 3 mm sections from the common carotid, bifurcation, and internal and external carotids were sectioned from whole arteries for all subjects, see Figure 1C. Samples were processed for histological staining as previously described.[25] Briefly, all sections were stepwise dehydrated and embedded in paraffin wax and sectioned in 7 μm thick slices prior to staining. All sections were stained with the following stains and their purpose is stated in parentheses: Haematoxylin & Eosin (H&E) (cell content), Verhoeff's elastin (elastin content), Picrosirius red (PLM; collagen content) with polarized light microscopy (collagen content), Alcian blue (glycosaminoglycan (GAG) content), and Alizarin red (calcium content), Figure 1D. The PLM for the Picrosirius red stained samples was conducted using an Olympus BX41 microscope with Ocular V2.0 software (Teledyne Photometrics, Tuscon, Arizona). All other stains had brightfield imaging done on an Aperio CS2 microscope with ImageScope software V12.3 (Leica Biosystems Imaging, Inc, Vista, CA).

Quantification of Histology

Quantification of histology measures were measured using QuPath[37] (version 0.2.3). Digital whole histology slides were imported into QuPath software where the following procedure was followed for Verhoeff's elastin, Alcian blue and Alizarin red: (1) the stain vector was set[38] for each histological stain, (2) the whole tissue region was delineated by thresholding the tissue slice from the background, and (3) the stained area fraction was then identified using further thresholding. Thresholds were kept consistent for each stain between all subjects. After this, both the images of the tissue region and the stained area

fraction were exported and brought into MATLAB where the percent content was calculated. Picrosirius red and the respective PLM images were analyzed similarly using an in-house built script described previously.[7] For cell density analysis, specific regions of interest were identified and exported from MATLAB, and subsequently manually drawn on the H&E image in QuPath where cell detection analysis was performed to yield 2D cell density measures. Quantitative measures were performed in regions of interest either determined by k-means clustering, see section k-Means Clustering, or by morphology, see section Morphological Regions of Interest.

Data Processing

Regions of Interest

Whole carotid arteries (n=8) were analyzed with visual confirmation of tissue integrity from histology, see Figure 1F. Regions with low signal-to-noise ratios and high residuals from the tensor model fitting were excluded from any of the following analyses to avoid any biasing the DTI metrics.[39] Specifically, pixels with signal below the 50% percentile in the non-diffusion weighted images were excluded as well as any pixels with a mean residual above the 99th percentile. Last, the mean MD of background PBS was used to remove PBS and yield the final tissue mask. Together, these criteria removed calcifications and air bubbles from all data (Figure S1). Mean FA and MD values were compared across the 8 vessels as well as mean values within individual anatomical regions of interest which were manually segmented. One mean value per vessel was compared when looking at entire subjects (mean across full field of view, 96 slices). When looking anatomically, the regions of interest were the common carotid (n=7), bifurcation (n=8), internal carotid (n=8), and external carotid (n=8). Similarly, 1 mean value per anatomical region (mean across all slices in each anatomical ROI; anatomical ROI size varied per subject but on average was 25 slices in the common, 22 in the bifurcation, and 30 in the branches) per subject was compared. The bifurcation was defined as the area where the common carotid transitioned from circular to oblique up to the apex of the bifurcation where the internal and external carotids split into individual branches. These anatomical regions where further separated into healthy and diseased regions of interest throughout the entire carotid. These delineations were manually drawn, with diseased regions classified as vessel wall regions that showed any deviation at all from the standard aged vessel wall as confirmed by histology (Figure 3; Figure S2). The mean metric of healthy and the mean metric of diseased ROIs within each anatomical ROI were compared (mean across all slices
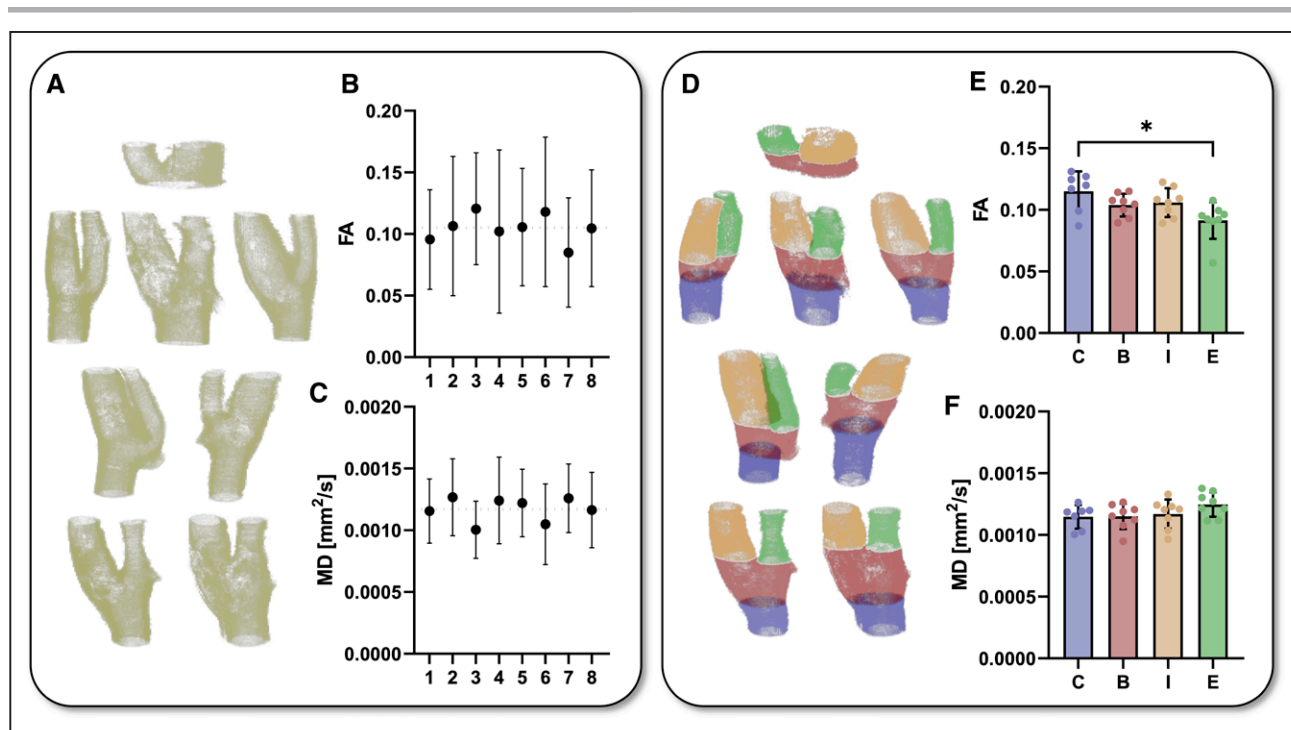
Figure 2. DTI metrics of n=8 cadaveric carotids.
A, 3D representations of the 8 individual carotid arteries. **B**, Fractional anisotropy (FA) and (**C**) mean diffusivity (MD) across the entire carotid for each subject. Each point represents the mean across the entire vessel (mean across entire field of view, 96 slices) with error bars showing the standard deviation. **C**, 3D representations of each carotid with the anatomical regions of interest color coded: common carotid in purple, bifurcation in red, internal carotid in orange, and external carotid in green. **D**, 3D representations of the 8 individual carotid arteries segmented by anatomical location. **E**, FA and (**F**) MD of separate anatomical regions of interest (C−common, B−bifurcation, I−internal carotid, E−external carotid). Each point represents the mean value across the slices in each specified anatomical region for individual vessels, n=8 for B, I, and E and n=7 for C. Significance tested by Kruskal-Wallis test, *P=0.0310.

within each anatomical ROI). Figure 3 presents 2 representative MRI cross-sections with corresponding histology: (Figure 3A) one representative healthy and (Figure 3B) one with both healthy and diseased ROIs. Figure S3 and Table 1 contain more detail on the relative size of the healthy and diseased regions within each vessel. Diseased regions were then normalized by their respective anatomical healthy region within the same subject to account for anatomical differences. For all regions, 1 mean value across the slices within the ROI and the standard deviation of FA and MD are reported.

Image Registration

For quantitative histological measures, common carotid (n=4 subjects, 1 MR slice per subject) histological slices (1 slice per stain, 5 stains) were registered to MRI. Registration was only performed on common carotid sections of 4 different subjects due to deformations in histological slices in more diseased regions of the carotids. Specifically, from Table 1, subjects 2, 3, 4, and 5 (left common carotid) were used for this part of the study (Figure S3 columns 2−5) yielding the inclusion of carotids which had type IV to type VI lesions. Anatomical landmarks (the apex of the bifurcation, the base of the common carotid at the 3D printed holder and notable anatomical features) allowed for manual matching of histology slices (0.495×0.495 μm) to a specific slice in high-resolution MR images. The tissue area of the identified MRI slice was then manually masked.[40] The corresponding brightfield histology image was then manually aligned to the identified high

resolution MRI slice by rotating and scaling providing an initial alignment for further calculated transformations. The manual alignment of histology to the high-resolution MRI was visually confirmed with reference to the anatomical landmarks prior to using Elastix[41,42] (version 5.0.1) to perform nonrigid registration based on BSpline deformation. Details of the registration can be found in Supplemental Material.

k-Means Clustering

A k-means clustering algorithm was used as an unsupervised segmentation tool on the common carotids which had histology registered to the MRI data (n=4 subjects, 1 MR slice per subject). The registered histology images mentioned above were imported into MATLAB alongside the parametric FA and MD maps for the specific slice. The elbow method was used to determine the appropriate number of clusters,[43] with k=5 proving to be sufficient for this data (Figure S4). Three different clustering inputs were investigated−FA, MD, and the combination of both FA and MD (Figure S5). Once the cluster regions were determined, mean FA and MD values were extracted for each region, along with the percent content of each of the 5 microstructural components for correlation analyses. It is worth noting that the background medium, in our case−PBS, was classified as a cluster so 4 regions are presented per sample. Quantitative histology, outlined above, was performed on the registered histology slices in the determined clusters in order to correlate microstructural components to DTI-derived metrics.
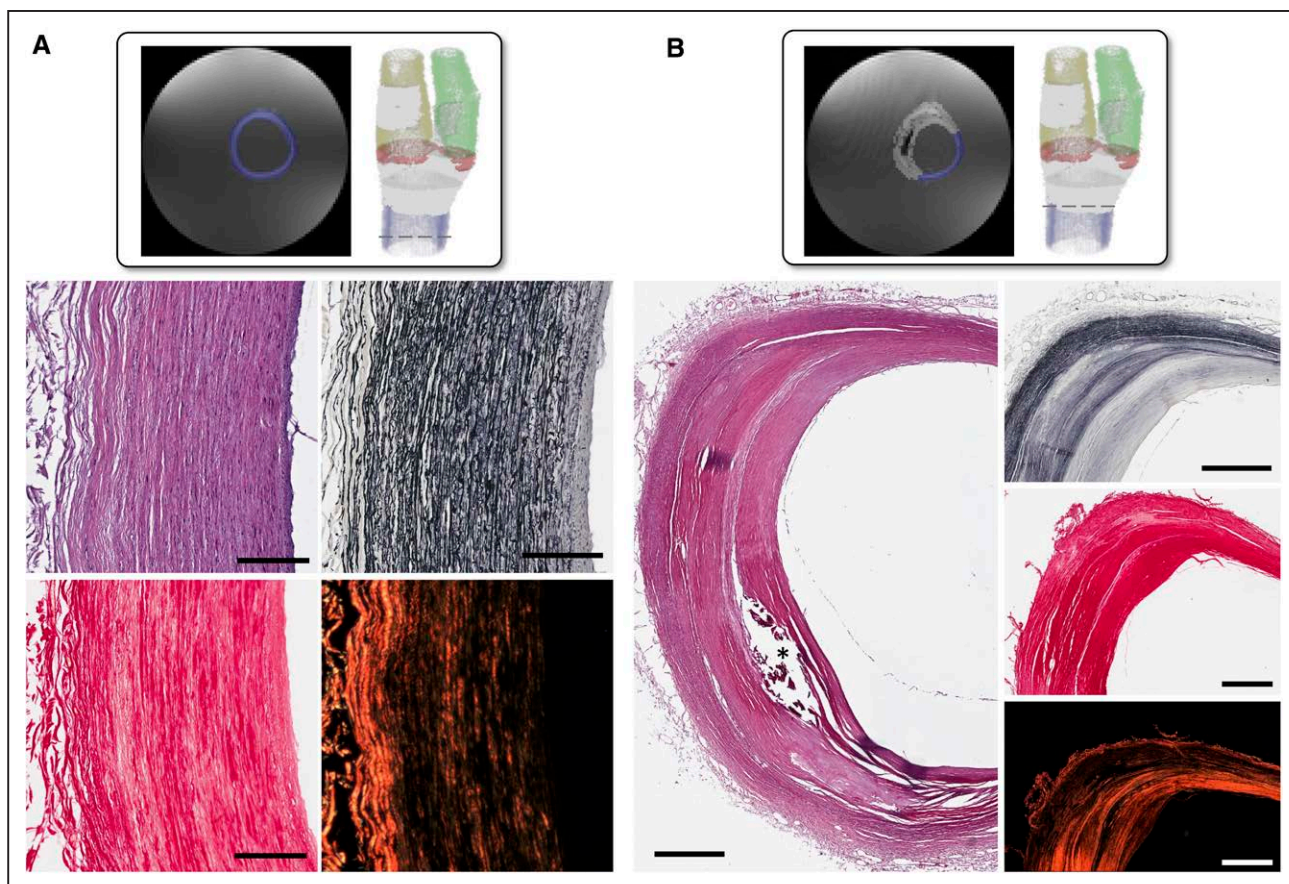
Figure 3. Representative healthy and diseased regions of interest.
A, One representative slice of common carotid with a blue mask conveying the healthy ROI. The dashed line in the 3D render shows the location of the slice. Representative H&E, Verhoeff's and picrosirius red (brightfield and PLM) of healthy common carotid. Scale bars are 200 µm. **B**, One representative slice of common carotid with a blue mask over the healthy ROI and the white mask over the diseased ROI. Similarly, representative histology of the various disease morphologies is shown. The asterisk marks where a calcification was. Scale bars are 1 mm. In the 3D renders, anatomical regions which are coloured (blue—common, red—bifurcation, yellow—internal, and green—external) are healthy ROIs, whereas grayed out regions are diseased. MR images are the non-diffusion weighted images.

Morphological Regions of Interest

The thickened intima (n=3) and the media (n=4) were identified and manually drawn on relevant DTI-registered H&E histology images (n=4 slices), Figure 1G. These morphological regions were then used to investigate DTI metrics and microstructural content between the registered histology and MR data in these 2 morphologies present in the common carotid.

Statistical Methods

Statistical analysis was performed using GraphPad Prism (Version 8). All data were tested for normality using D'Agostino-Pearson normality tests and equality of group variances with Brown-Forsythe ANOVAs. If the data did not pass normality (alpha=0.05) or had too small a sample size (n<8), nonparametric tests were used. All normal data passed equal variances tests. For mean FA and MD in the different anatomical locations, the nonparametric Kruskal-Wallis test was used. Comparing healthy and diseased ROIs across the 8 vessels, unpaired *t*-tests were used as the data passed normality and equal variance tests. A 2-way ANOVA was used for investigating differences between healthy and diseased ROIs with respect to anatomical location. Pearson correlations were used

to determine the relationship between microstructural components and DTI metrics. Correlation coefficients (r) below 0.3 were considered a weak correlation, up to 0.7 a moderate correlation and above 0.7 a strong correlation.[44] Last, nonparametric Mann-Whitney tests were used when investigating morphological ROIs in the common carotids due to limited sample numbers (n=3 and 4). Statistical significance was considered when $P<0.05$.

RESULTS

DTI Metrics of Cadaver Carotids

Figure 2A shows 3D representations of the n=8 carotids used in this study alongside the mean (Figure 2B) FA, and (Figure 2C) MD in each carotid for the whole sample (1 mean value per vessel). The mean FA between all vessels was 0.105±0.0511 and the mean MD was 0.00117±0.000292 mm^2/s (both marked by dotted lines). Anatomical delineations of the common carotid, bifurcation, internal carotid, and external carotid can be seen in 3D renders in Figure 2D.

The mean FA and MD for all subjects (1 mean value per vessel, n=8 for the bifurcation, internal and external, n=7 for the common) are presented in Figure 2E and 2F. The common (0.115±0.0499) had the highest anisotropy and was significantly higher (*P=0.0310) than that in the external carotid (0.0914±0.0392). The mean FA at the bifurcation was 0.104±0.0528 and 0.106±0.0529 in the internal carotid. For MD no significant differences were seen between anatomical regions (common: 0.00115±0.00006 mm²/s, bifurcation: 0.00115±0.00005 mm²/s, internal: 0.00117±0.00003 mm²/s, and external: 0.00125±0.00006 mm²/s).

All subjects included in this study showed varying signs of atherosclerosis despite the fact that cardiovascular disease was not implicated as a cause of death for any subject, see Figure S3. Histology was used to confirm healthy and diseased delineated regions for examination; however, it is important to remember this healthy tissue is aged. Figure 3 shows representative 3D renders of a vessel with both anatomical and healthy and diseased regions shown. Figure 3A shows examples of healthy vessel wall histology from the dashed line location in the 3D render. Figure 3B shows histology with various diseased morphologies present.

Diseased regions, confirmed by histology as seen in Figure 3, were compared against healthy tissue. Figure 4A and 4D presents the mean healthy and diseased FA and MD values for each subject (n=8). The mean FA measured within healthy regions was 0.0996±0.0154 while the mean FA diseased regions was slightly higher at 0.109±0.0123. The MD measured in healthy regions, 0.00123±0.00009 mm²/s, was significantly higher (*P=0.0406) than that measured in diseased regions, 0.00112±0.00008 mm²/s. When investigating healthy and diseased regions of interest based on anatomical location, there was a significance difference in (Figure 4B) FA based on anatomical location (*P=0.0136) and a significant difference between healthy and diseased regions for (Figure 4E) MD (###P=0.0005). Different morphologies included in this diseased grouping can be seen in Figure S9 alongside representative MRI slices. Diseased regions were normalized by their respective healthy anatomical region per subject and normalized FA and MD values are presented in Figure 4C and 4F. Deviation from a value of 1 signifies how much the diseased tissue differs from healthy tissue in that specific region. For example, when looking at subject 7 in Figure 4C all anatomical regions show a value > 1—indicating that the FA was higher in diseased regions than healthy. The opposite is seen in subject 4. The normalized MD values presented in Figure 4F are all below 1, indicating that all diseased tissue, regardless of subject or anatomical location, had a lower MD value than the healthy tissue. Some subjects have < 4 anatomical regions presented in Figure 4C and 4F—indicating

that the missing anatomical regions were either entirely healthy or diseased. Details can be seen in Table S1.

Quantitative Histology and DTI Metrics

DTI Metrics and Microstructural Components

DTI metrics and quantitative histology were investigated within the common carotids of 4 subjects. Figure 5 presents the strong and moderate correlations for FA in the first column (Figure 5A, 5C, 5E) and MD (Figure 5B, 5D, 5F) in the second column against different microstructural components. Different rows correspond to the different clustering inputs: FA input is presented on the top row (Figure 5A and 5B), MD input in the middle (Figure 5C and 5D) and both FA and MD on the third row (Figure 5E and 5F). Detailed summaries of the Pearson's correlations are presented in Tables 2 and 3 for FA and MD, respectively. Elastin content had a significant and strong positive correlation with FA regardless of clustering input, r_{FA}=0.7197 (P=0.0017), r_{MD}=0.7970 (P=0.0002), r_{FA+MD}=0.7140 (P=0.0010). Similarly, elastin had a significant and strong negative correlation with MD with all inputs, r_{FA}=−0.7996 (P=0.0002), r_{MD}=−0.8266 (P<0.0001), r_{FA+MD}=−0.8030 (P=0.0002). Collagen content had a moderate correlation with both FA and MD regardless of input. GAG content had a moderate negative correlation with FA when FA and FA+MD were clustering inputs, r_{FA}=−0.5551 and r_{FA+MD}=−0.4649, respectively. Cell density was found to have a moderate negative correlation with FA when FA and MD were clustering inputs, r_{FA}=−0.4836 and r_{MD}=−0.4453. Cell density had moderate positive correlations with MD for all inputs, r_{FA}=0.3035, r_{MD}=0.4823, and r_{FA+MD}=0.4475. Weak to no correlations can be seen in Figure S6 and are detailed in Tables 1 and 2. Additionally, correlations between microstructural components can be found in Figures S7 and S8 and details of their Pearson's correlations in Tables S2 through S5.

DTI Metrics and Atherosclerotic Morphologies

DTI metrics between specific atherosclerotic morphologies were investigated using the registered histology. In 4 subjects, thickened intima was present in common carotids (n=3) and compared with the media (n=4). Figure 6A presents the media and thickened intima in a H&E cross section and the mean (Figure 6B) FA and (Figure 6C) MD for both regions as well as the (Figure 6D) cell density, (Figure 6E) elastin, (Figure 6F) collagen, (Figure 6G) GAG, and (Figure 6H) calcium content. While not significant, FA, cell density and elastin content were all higher in the vessel media than in the thickened intima and the MD was lower in the vessel media. Figure 6I shows the differences in total microstructural content between the 2 regions for elastin (black), collagen (red), GAG (blue), and calcium (beige). Cell density was excluded from total content in Figure 6I as it is a density unlike the other components which are
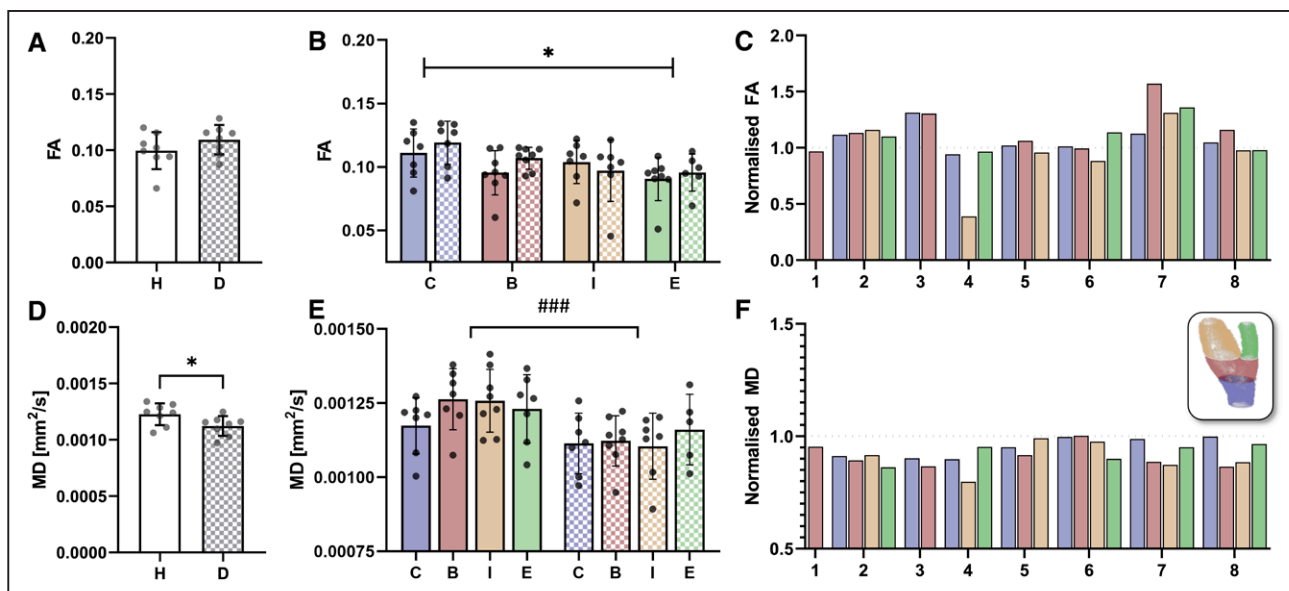
Figure 4. Diffusion tensor imaging metrics in healthy and diseased ROIs.
A, fractional anisotropy (FA) and (**D**) mean diffusivity (MD) in healthy (solid bars) and diseased (checkered bars) ROIs of each vessel, n=8, regardless of anatomical location. Significance tested by unpaired t-tests, in **D**. *P=0.0406. **B**, FA and (**E**) MD in healthy and diseased ROIs within specific anatomical locations. Significance was determined by a 2-way ANOVA, *P=0.0136 between anatomical locations for FA and ###P=0.0005 between healthy and diseased regions for MD (n=7 healthy ROIs in the common, bifurcation and internal and n=8 in the external carotid; n=7 diseased ROIs in the common and internal carotid, n=8 in the bifurcation, and n=6 in the external carotid). Pairwise comparisons are non-significant. **C**, Normalized FA and (**F**) MD (diseased by healthy) for n=8 subjects. Missing bars mean the anatomical region was either completely healthy or diseased. Insert in **F** shows visual representation of the different anatomical ROIs in 1 vessel.

represented by a stained area fraction. The total stained area fraction of all components for thickened intima was 94.59% and 98.26% stained for the media.

Tractography of Cadaveric Carotids

Tractography revealed varying degrees of microstructural alignment within each subject, shown in Figure 7. All subjects showed some degree of circumferential alignment; however, some showed significant axial alignment and disorganisation, Figure 7G and 7H. Regions of advanced disease, such as calcifications, were colocalized with incoherent and non-continuous tracts in some subjects.

DISCUSSION

DTI Metrics of Cadaver Carotids

DTI has been used to investigate arterial tissue in both ex vivo[25,26,28,45–47] and in vivo[29] studies. Studies specifically investigating DTI metrics in human atherosclerotic tissue are limited. When investigating the potential of in vivo DTI, Opriessnig et al[29] found a strong negative correlation between FA and patient age, with a mean age of the 12 subjects being 38 years old. All subjects in the current study were above 70 years old and low anisotropy was apparent across all carotids. The FA is significantly lower in these aged samples than in previous studies investigating healthy porcine arterial tissue.[25–27] No subjects in this study died of cardiovascular disease;

however, there were varying signs of atherosclerosis present for all subjects. While it is not possible to know for sure these subjects were asymptomatic, the signs of advanced disease present in most subjects combined with noncardiovascular-related CODs suggests it was in fact the silent progression of atherosclerosis. Based on percent stenosis alone, it is likely some of these subjects would have been recommended for an intervention; however, we know atherosclerosis was not the COD for any of the subjects. Vascular aging is characterized by the loss of arterial elasticity and reduced arterial compliance,[48] which may be an early cardiovascular risk indicator.[49] The imbalance of microstructural components in the vessel wall, governed by elastin fragmentation, immune cell infiltration, cytokine accumulation and collagen deposition, coupled with chronic inflammation, dysregulation of cellular homeostatic systems and senescence inhibits arterial relaxation, changing the mechanical environment and ultimately allowing for atherosclerotic lesion progression.[50] Therefore, it is possible that the significant drop in FA present in all subjects, regardless of anatomical location or healthy or diseased ranking, could be an early indicator for early vessel wall degradation.

When looking at the samples without considering the health of the tissue, a significant difference was found between the FA of the common carotid and external carotid. However, when healthy and diseased regions were delineated, the MD was significantly lower in diseased areas. It is important to note that these diseased regions were nonspecific and included many different
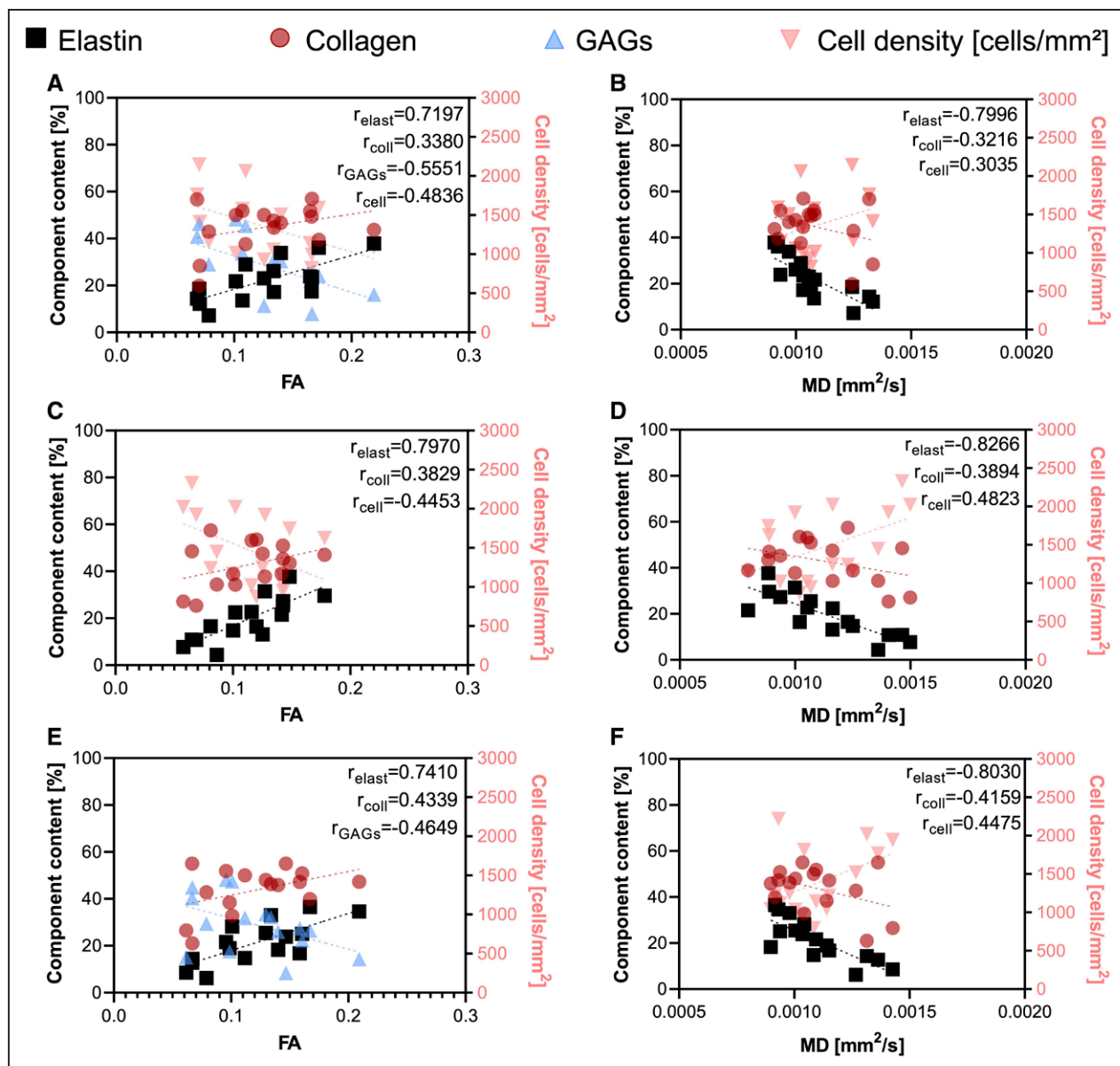
Figure 5. Correlation of microstructural components, determined by quantitative histology, and diffusion tensor imaging (DTI) metrics based on clustering input,
namely (**A** and **B**) fractional anisotropy (FA), (**C** and **D**) mean diffusivity (MD), and (**E** and **F**) FA and MD. DTI metrics and elastin content displayed strong correlations via Pearson correlations regardless of clustering input. Collagen, GAGs, and cell content showed moderate correlations with DTI metrics depending on clustering input. Weak correlations can be seen in Figure S6.

morphologies, as evidenced in Figure 3 and Figure S3. While some atherosclerotic morphologies might show disorganization in the changing vessel wall, highly aligned fiber patterns either encircling, attached to and/or pushed around calcifications have been seen.[51] As seen in the normalized FA values (Figure 4C), there is no clear trend suggesting either specific microstructural changes or disease morphologies are present across all subjects. It is important to note this could be due to the averaging of opposing trends, hiding any healthy versus diseased specific effects. While outside the scope of the current study, it is possible that further identifying and classifying these diseased regions could highlight clearer

trends between DTI metrics and specific morphologies. Figure S9 shows these qualitative differences. Ultimately, in the future, registration with histology including multiple disease morphologies would help answer this remaining question. Additionally, the MD was significantly lower in diseased compared with healthy regions. While previous work in arterial tissue has suggested that increased cell content contributes to a decreased MD,[25] lipid has been shown to reduce diffusivity and is lower when compared with fibrous plaque tissue and vessel wall in vivo.[52,53] The MD of healthy arterial tissue found in this study agrees well with previously reported values of normal carotid wall[52] and the diseased MD falls between reported

Table 2. Summary of Pearson's Correlations Between FA and Microstructural Components

	Input	r	95% CI	R²	P Value
Elastin	FA	0.7197	0.3482–0.8958	0.5179	0.0017*
	MD	0.7970	0.4980–0.9266	0.6351	0.0002†
	FA+MD	0.7410	0.3876–0.9045	0.5490	0.0010*
Collagen	FA	0.3380	−0.1894–0.7141	0.1142	0.2004
	MD	0.3829	−0.1393–0.7384	0.1466	0.1433
	FA+MD	0.4339	−0.07875–0.7650	0.1883	0.0931
GAG	FA	−0.5551	−0.8240 to −0.08191	0.3081	0.0256‡
	MD	−0.2004	−0.6332–0.3279	0.04017	0.4567
	FA+MD	−0.4649	−0.7807–0.04008	0.2161	0.0696
Calcium	FA	−0.1628	−0.6093–0.3622	0.02649	0.5470
	MD	0.06397	−0.4459–0.5425	0.004092	0.8139
	FA+MD	−0.08352	−0.5562–0.4300	0.006975	0.7585
Cell density	FA	−0.4836	−0.7899–0.01593	0.2339	0.0577
	MD	−0.4453	−0.7709–0.06467	0.1983	0.0839
	FA+MD	−0.2060	−0.6367–0.03227	0.04243	0.4441

FA indicates fractional anisotropy; and MD, mean diffusivity.
Significance: *$P<0.01$; †$P<0.001$; ‡$P<0.05$.

values for lipid core and fibrous plaque.[52] Histological deformation prevented the registration of histology past the common carotid in this study; however, lipid rich cores can be seen in H&E-stained slices from diseased regions (Figure S9).

## DTI Metrics and Microstructural Components

Following image registration and the use of an unsupervised segmentation algorithm, a strong correlation was found between both FA and MD and elastin. Regardless of clustering input, there was a strong correlation with elastin. Elastin fragmentation is not only evident in vascular aging but also present in the earliest signs of atherosclerosis. Its complete depletion has previously shown a drastic impact on DTI metrics[25]; however, it was not fully understood the impact elastin had within physiological tissue conditions. From initial endothelial dysfunction to formation of atherosclerotic lesions, the extracellular matrix is drastically modified—of particular interest here are the elastic fibers.[54] Elastin chains rarely turnover due to their stability and longevity, so any damage, such as proteolytic degradation from lipid and calcium deposits, tends to be irreversible. The quality and quantity

Table 3. Summary of Pearson's Correlations Between MD and Microstructural Components

	Input	r	95% CI	R²	P Value
Elastin	FA	−0.7996	−0.9276 to −0.5034	0.6394	0.0002*
	MD	−0.8266	−0.9380 to −0.5606	0.6832	<0.0001†
	FA+MD	−0.8030	−0.9289 to −0.5104	0.6448	0.0002†
Collagen	FA	−0.3216	−0.7049–0.2071	0.1034	0.2245
	MD	−0.3894	−0.7419–0.1371	0.1516	0.1360
	FA+MD	−0.4159	−0.7558–0.1006	0.1729	0.1091
GAG	FA	0.2783	−0.2522–0.6802	0.07744	0.2956
	MD	−0.01048	−0.5036–0.4878	0.0001099	0.9693
	FA+MD	0.1772	−0.3491–0.6186	0.03141	0.5114
Calcium	FA	0.03007	−0.4727–0.5181	0.0009043	0.9120
	MD	−0.1261	−0.5852–0.3943	0.01589	0.6418
	FA+MD	−0.04391	−0.5281–0.4618	0.001928	0.8717
Cell density	FA	0.3035	−0.2262–0.6947	0.09214	0.2531
	MD	0.4823	−0.01759–0.7893	0.2326	0.0585
	FA+MD	0.4475	−0.06189–0.7720	0.2003	0.0822

FA indicates fractional anisotropy; and MD, mean diffusivity.
Significance: *$P<0.001$; †$P<0.0001$.
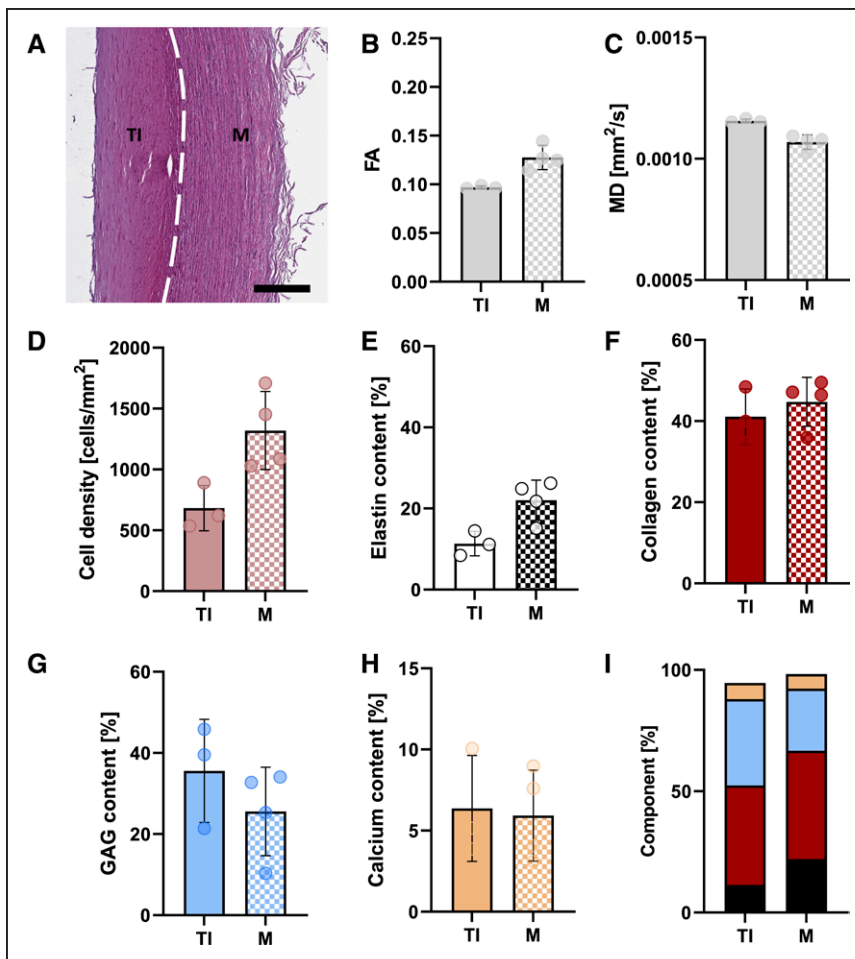
Figure 6. Morphological assessment of diffusion tensor imaging (DTI) metrics.
A, Registered histology informed the presence of the thickened intima (TI) and media (M) within the common carotids. Scale bar 300 um. **B**, Fractional anisotropy (FA) and (**C**) mean diffusivity (MD) in the media and thickened intima. **D** through **H**, Microstructural differences between the media and thickened intima. **I**, Collagen (red), elastin (black), GAGs (blue), and calcium (beige) parts of a whole for both thickened intima and media. Cell content was not included as it is a density rather than stained area fraction. Total area for thickened intima was 94.59% and 98.26% stained for the media. No significant differences were found (**B**–**H**) using Mann-Whitney tests; n=4 media and n=3 for thickened intima.

of elastin is a good indicator of vessel wall health, and therefore the strong correlation it has with DTI metrics is very promising. Furthermore, any pathologies associated with the focal loss of elastin, elastin synthesis, or altered turnover—such as Williams Syndrome,[55] cutis laxa,[56] or aneurysms[54]—may be promising, advantageous avenues for the application of DTI beyond carotid atherosclerosis.

Outside of the strong correlation with elastin content, moderate correlations were found between FA and collagen, GAG content, and cell density when FA was used as a clustering input. As the elastin and collagen content decrease and GAG and cell content increase, the FA decreases (Figure 5A). While it seems clear that elastin content showed the most dominate correlation with DTI metrics when using k-means clustering segmentation, it did not identify known morphologies with decreased elastin content—such as the thickened intima or lipid core. However, the combination of multiple microstructural components influenced measurable anisotropy. Collagen content and cell density both showed moderate correlations with MD regardless of clustering input and were correlated with each other for all inputs. As the MD increased, collagen content decreased, and cell density increased. Additionally, while calcium showed no correlation with DTI metrics it did maintain a moderate negative correlation

with collagen content. It has been shown that collagen type II content is significantly higher around calcifications[57]; however, the calcium content in this study signified calcium deposits, potentially preceding microcalcifications, rather than calcifications themselves. It appears that the unsupervised segmentation of DTI metrics for common carotids does not yield morphological regions and was instead highly correlated to elastin specifically. For example, no regions identified the thickened intima (present in 3 subjects)—with decreased cell and elastin content but increased GAG content. The relationships between the other microstructural components in these automatically segmented regions showed moderate correlations at best, furthering the conclusion that the clusters were driven by the strong relationship between FA, MD, and elastin.

DTI Metrics and Atherosclerotic Morphologies

After looking for fundamental microstructurally driven changes in FA and MD, distinct atherosclerotic morphologies were investigated. In the aged common carotids, the only atherosclerotic morphology present within the vessel wall was the thickened intima—classified as an intermediate lesion, type III, in plaque development.[58] While DTI metrics were not found to
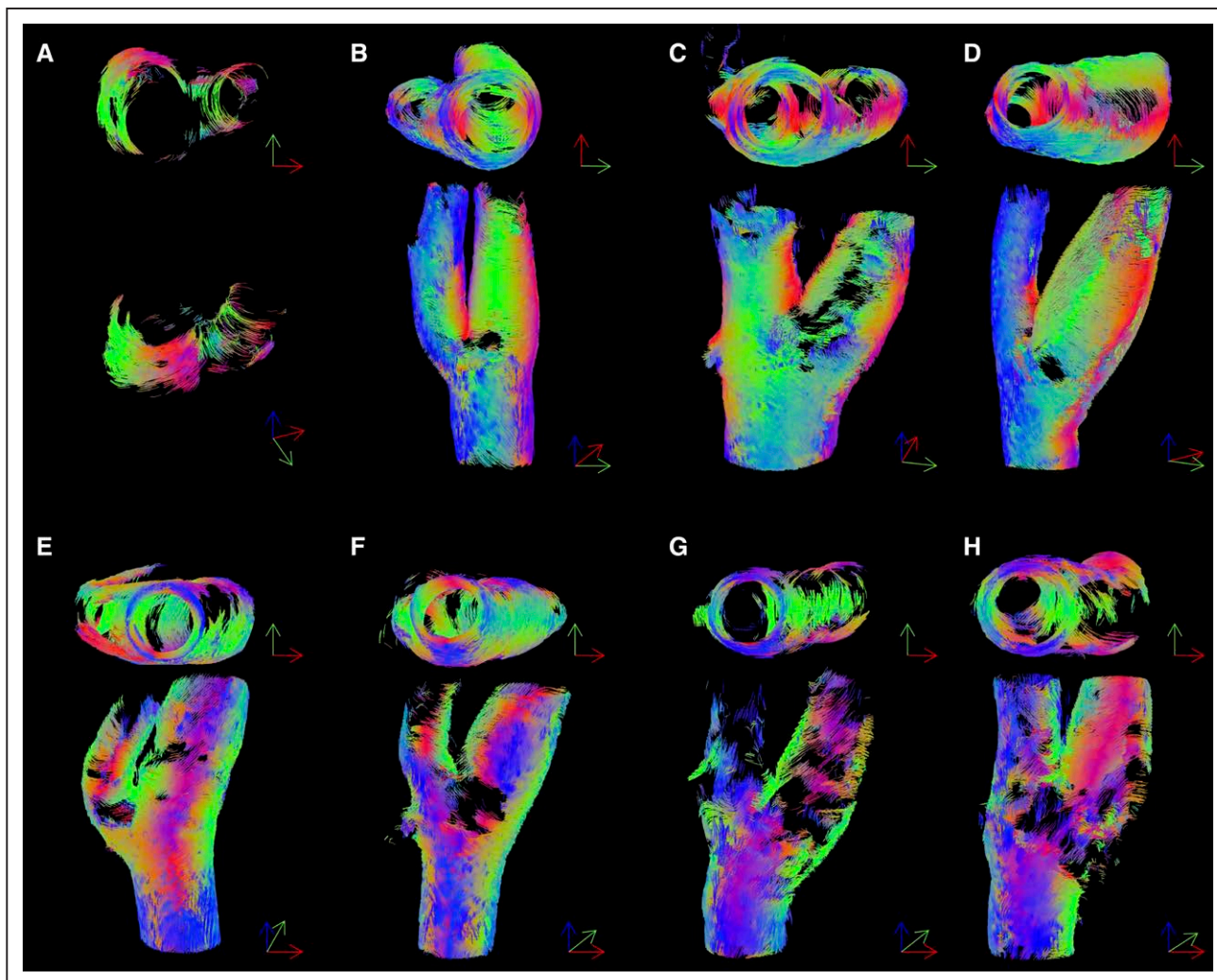
Figure 7. Tractography of cadaveric carotid arteries.
Top row of **A**–**H** shows an axial view of the carotids, looking from the base of the common into the lumen towards the bifurcation and branches. Green-red tracts represent in-plane alignment (circumferential) while blue tracts are indicative of axial alignment.

be sensitive to individual microstructural changes outside of elastin (Figure 5; Tables 2 and 3), they seem to be sensitive to bulk microstructural changes in atherosclerotic morphologies, as evidenced in Figure 6. The decreased FA and increased MD in the thickened intima corroborates the strong correlation observed between elastin and these metrics and previous knowledge on the importance of cell content.[25] The decreased cell and elastin content characterize the thickened intima and are distinguishable from the vessel media. Cell content in this study was not investigated with respect to specific cell types, smooth muscle cells or macrophages, but the cell density in the thickened intima is comparable to that seen in type II lesions.[20] There was an increase in GAG content that suggests that it's possible these morphologies are an intermediate step between GAG rich fatty streaks,[59] type II, and type III lesions. While previous studies have used diffusion weighted imaging to identify advanced lipid necrotic cores,[52,53,60] to the authors' knowledge,

this is the first to use DTI to identify early-stage atherosclerosis in human carotid arteries.

Limitations

While the results of this study are promising, there are limitations to be considered. Most notably, the number of diffusion directions is at the lower limit and outside the optimal ratio of unweighted to weighted diffusion scans.[61] Given the unexpected diseased nature of the subjects used in this study, it is possible the limited number of directions did not allow for an adequate representation of the microstructural organization in areas of advanced disease. However, tractography results were able to show overall representations of organization, or lack thereof, for individual subjects. While the fixed nature of the carotids was ideal for the long scan times that come with 3D sequences and facilitated an in-depth look at the microstructure, it is worth commenting on the embalming process and possible variations in the

embalming of different subjects. The time from embalming to excising could not be controlled for; however, after excision all carotids were stored in PBS. Additionally, the extreme scan times in this study are not clinically feasible; however, other studies have identified different DTI acquisition techniques which speed up acquisition.[26,27,29] While there is still work to be done on the clinical translation of this work, the authors think this study highlights the potential of this imaging technique for clinical use. Future work will focus on bringing this imaging method to more clinically relevant fresh tissue. It is also worth mentioning that dimensions of different plaque components may change during embalming, freezing, and thawing. While the samples were never frozen, it is important to note that the phase properties of some cholesterol esters may alter between liquid and crystalline phases near body temperature.[62] Specifically, for the liquid phase the melting point is 44 °C; however, typically in plaque tissue the presence of multiple different lipids lowers this melting temperature.[63] All samples were stored at 4 °C and allowed to equilibrate to room temperature prior to scanning at room temperature (approx. 25 °C). All quantitative microstructural measures were taken from 2D histological slices and compared with 3D MRI volumes, but this was kept consistent across all samples. Lastly, between the registration of MR images and histology, there are distortions that occur in histological processing, which could affect how accurately and precisely the histological slice can be registered to the MRI slice.[64] Additionally, this study did not look at inflammation histologically; however, inflammation has been shown to be indicative of increased stress in coronary plaques[5] and should be investigated in carotid plaques in the future.

CONCLUSIONS

In this work, human carotid arteries were imaged by ex vivo DTI and investigated as whole carotids, microstructurally and morphologically. An across-the-board low anisotropy was seen in all aged subjects highlighting the potential for assessing vessel integrity prior to atherosclerotic lesion development. The MD showed a sensitivity to unspecific advanced regions of disease. Microstructurally, elastin content showed a strong correlation with FA and MD when using unsupervised automatic segmentation regardless of clustering input. Lastly, early atherosclerotic features are distinguishable from the vessel wall by both FA and MD. Together, these different investigations point to the potential of DTI metrics as non-invasive biomarkers to identify atherosclerotic characteristics in carotid arteries, at early onset and late-stage lesion development.

ARTICLE INFORMATION

Affiliations

Trinity Centre for Biomedical Engineering, Trinity Biomedical Sciences Institute (B.T., A.J.S., C.K., C.L.), Department of Mechanical, Manufacturing and Biomedical Engineering, School of Engineering (B.T., A.J.S., C.L.), Trinity College Institute of Neuroscience (C.K.), and Advanced Materials and Bioengineering Research Centre (AMBER), Royal College of Surgeons in Ireland and Trinity College Dublin (C.L.), Ireland. Department of Medical Physics and Clinical Engineering, St. Vincent's University Hospital, Dublin, Ireland (A.J.S.).

Disclosures

None.

Supplemental Material

Expanded materials and methods
Figures S1–S9
Tables S1–S5
References 23, 25, 30–35

REFERENCES

1. Bentzon JF, Otsuka F, Virmani R, Falk E. Mechanisms of plaque formation and rupture. *Circ Res*. 2014;114:1852–1866. doi: 10.1161/CIRCRESAHA.114.302721
2. Davies MJ, Richardson PD, Woolf N, Katz DR, Mann J. Risk of thrombosis in human atherosclerotic plaques: Role of extracellular lipid, macrophage, and smooth muscle cell content. *Br. Heart J*. 1993;69:377–381. doi: 10.1136/hrt.69.5.377
3. Kwak BR, Bäck M, Bochaton-Piallat ML, Caligiuri G, Daemen MJAP, Davies PF, Hoefer IE, Holvoet P, Jo H, Krams R. et al. Biomechanical factors in atherosclerosis: Mechanisms and clinical implications. *Eur Heart J*. 2014;35:3013–20, 3020a. doi: 10.1093/eurheartj/ehu353
4. Kolodgie FD, Burke AP, Farb A, Gold HK, Yuan J, Narula J, Finn AV, Virmani R. The thin-cap fibroatheroma: a type of vulnerable plaque the major precursor lesion to acute coronary syndromes. *Curr. Opin. Cardiol*. 2001;16:285–292. doi: 10.1097/00001573-200109000-00006
5. Hallow KM, Taylor WR, Rachev A, Vito RP. Markers of inflammation collocate with increased wall stress in human coronary arterial plaque. *Biomech Model Mechanobiol*. 2009;8:473–486. doi: 10.1007/s10237-009-0151-8
6. Campbell IC, Suever JD, Timmins LH, Veneziani A, Vito RP, Virmani R, Oshinski JN, Taylor WR. Biomechanics and inflammation in atherosclerotic plaque erosion and plaque rupture: Implications for cardiovascular events in women. *PLoS One*. 2014;9:e111785. doi: 10.1371/journal.pone.0111785
7. Johnston RD, Gaul RT, Lally C. An investigation into the critical role of fibre orientation in the ultimate tensile strength and stiffness of human carotid plaque caps. *Acta Biomater*. 2021;124:291–300. doi: 10.1016/j.actbio.2021.02.008
8. Nagai Y, Kitagawa K, Sakaguchi M, Shimizu Y, Hashimoto H, Yamagami H, Narita M, Ohtsuki T, Hori M, Matsumoto M. Significance of earlier carotid atherosclerosis for stroke subtypes. *Stroke*. 2001;32:1780–1785. doi: 10.1161/01.str.32.8.1780
9. Wasserman BA, Wityk RJ, Trout HH, Virmani R. Low-grade carotid stenosis: looking beyond the lumen with MRI. *Stroke*. 2005;36:2504–2513. doi: 10.1161/01.STR.0000185726.83152.00
10. Gaba K, Ringleb PA, Halliday A. Asymptomatic carotid stenosis: intervention or best medical therapy?. *Curr Neurol Neurosci Rep*. 2018;18:1–9. doi: 10.1007/s11910-018-0888-5

11. Montenegro A, Rodriguez HP, Mantilla DK, Balderrama J, Diaz C, Zenteno M. Update on diagnostic approach of carotid disease: from stenosis to atherosclerotic plaque morphology. *Interdiscip Neurosurg Adv Tech Case Manag*. 2021;26:1–5. doi: 10.1016/j.inat.2021.101363

12. Clarke SE, Hammond RR, Mitchell JR, Rutt BK. Quantitative assessment of carotid plaque composition using multicontrast MRI and registered histology. *Magn Reson Med*. 2003;50:1199–1208. doi: 10.1002/mrm.10618

13. Morrisett J, Vick W, Sharma R, Lawrie G, Reardon M, Ezell E, Schwartz J, Hunter G, Gorenstein D. Discrimination of components in atherosclerotic plaques from human carotid endarterectomy specimens by magnetic resonance imaging ex vivo. *Magn Reson Imaging*. 2003;21:465–474. doi: 10.1016/s0730-725x(02)00643-4

14. Lopez Gonzalez MRR, Foo SYY, Holmes WMM, Stewart W, Muir KWW, Condon B, Welch G, Forbes KPP. Atherosclerotic carotid plaque composition: a 3t and 7t mri-histology correlation study. *J Neuroimaging*. 2016;26:406–413. doi: 10.1111/jon.12332

15. Viereck J, Ruberg FL, Qiao Y, Perez AS, Detwiller K, Johnstone M, Hamilton JA. MRI of atherothrombosis associated with plaque rupture. *Arterioscler Thromb Vasc Biol*. 2005;25:240–245. doi: 10.1161/01.ATV.0000149673.00564.0a

16. Jiang Y, Zhu C, Peng W, Degnan AJ, Chen L, Wang X, Liu Q, Wang Y, Xiang Z, Teng Z. et al. Ex-vivo imaging and plaque type classification of intracranial atherosclerotic plaque using high resolution MRI. *Atherosclerosis*. 2016;249:10–16. doi: 10.1016/j.atherosclerosis.2016.03.033

17. Shinnar M, Fallon JT, Wehrli S, Levin M, Dalmacy D, Fayad ZA, Badimon JJ, Harrington M, Harrington E, Fuster V. The diagnostic accuracy of ex vivo mri for human atherosclerotic plaque characterization. *Arterioscler Thromb Vasc Biol*. 1999;19:2756–2761. doi: 10.1161/01.atv.19.11.2756

18. Harteveld A, Denswil NP, Siero JCW, Zwanenburg JJM, Vink A, Pouran B, Spliet WGM, Klomp DWJ, Luijten PR, Daemen MJ. et al. Quantitative intracranial atherosclerotic plaque characterization at 7T MRI: an ex vivo study with histologic validation. *Am. J Neuroradiol*. 2016;37:802–810. doi: 10.3174/ajnr.A4628

19. Karmonik C, Basto P, Morrisett JD. Quantification of carotid atherosclerotic plaque components using feature space analysis and magnetic resonance imaging. *Annu Int Conf IEEE Eng Med Biol Proc*. 2006;3102–3105. doi: 10.1109/IEMBS.2006.260318

20. Orekhov AN, Andreeva ER, Andrianova IV, Bobryshev YV. Peculiarities of cell composition and cell proliferation in different type atherosclerotic lesions in carotid and coronary arteries. *Atherosclerosis*. 2010;212:436–443. doi: 10.1016/j.atherosclerosis.2010.07.009

21. Barnes MJ, Farndale RW. Collagens and atherosclerosis. *Exp Gerontol*. 1999;34:513–525. doi: 10.1016/s0531-5565(99)00038-8

22. Kramsch DM, Franzblau C, Hollander W. The protein and lipid composition of arterial elastin and its relationship to lipid accumulation in the atherosclerotic plaque. *J Clin Invest*. 1971;50:1666–1677. doi: 10.1172/JCI106656

23. Stone AJ, Tornifoglio B, Johnston RD, Shmueli K, Kerskens C, Lally C. Quantitative susceptibility mapping of carotid arterial tissue ex vivo: assessing sensitivity to vessel microstructural content. *Magn Reson Med*. 2021;86:2512–2527. doi: 10.1002/mrm.28893.

24. Azuma M, Maekawa K, Yamashita A, Yokogami K, Enzaki M, Khant ZA, Takeshima H, Asada Y, Wang Y, Hirai T. Characterization of carotid plaque components by quantitative susceptibility mapping. *Am. J Neuroradiol*. 2020;41:310–317. doi: 10.3174/ajnr.A6374

25. Tornifoglio B, Stone AJ, Johnston RD, Shahid SS, Kerskens C, Lally C. Diffusion tensor imaging and arterial tissue: establishing the influence of arterial tissue microstructure on fractional anisotropy, mean diffusivity and tractography. *Sci Rep*. 2020;10:1–12. doi: 10.1038/s41598-020-77675-x

26. Shahid SS, Gaul RT, Kerskens C, Flamini V, Lally C. Quantifying the ultrastructure of carotid arteries using high-resolution micro-diffusion tensor imaging - comparison of intact versus open cut tissue. *Phys Med Biol*. 2017;62:8850–8868. doi: 10.1088/1361-6560/aa9159

27. Shahid SS, Johnston RD, Smekens C, Kerskens C, Gaul R, Tornifoglio B, Stone AJ, Lally C. Exploring arterial tissue microstructural organization using non-Gaussian diffusion magnetic resonance schemes. *Sci Rep*. 2021;11:1–13.doi: 10.1038/s41598-021-01476-z

28. Akyildiz AC, Chai CK, Oomens CWJ, van der Lugt A, Baaijens FPT, Strijkers GJ, Gijsen FJH. 3D fiber orientation in atherosclerotic carotid plaques. *J. Struct. Biol*. 2017;200:28–35. doi: 10.1016/j.jsb.2017.08.003

29. Opriessnig P, Mangge H, Stollberger R, Deutschmann H, Reishofer G. In vivo cardiovascular magnetic resonance of 2D vessel wall diffusion anisotropy in carotid arteries. *J Cardiovasc Magn Reson*. 2016;18:1–9.

30. Veraart J, Novikov DS, Christiaens D, Ades-aron B, Sijbers J, Fieremans E. Denoising of diffusion MRI using random matrix theory. *Neuroimage*. 2016;142:394–406. doi: 10.1016/j.neuroimage.2016.08.016

31. Kellner E, Dhital B, Kiselev VG, Reisert M. Gibbs-ringing artifact removal based on local subvoxel-shifts. *Magn Reson Med*. 2016;76:1574–1581. doi: 10.1002/mrm.26054

32. Tournier JD, Smith R, Raffelt D, Tabbara R, Dhollander T, Pietsch M, Christiaens D, Jeurissen B, Yeh CH, Connelly A. MRtrix3: A fast, flexible and open software framework for medical image processing and visualisation. *Neuroimage*. 2019;202:116137. doi: 10.1016/j.neuroimage.2019.116137

33. Stejskal EO, Tanner JE. Spin diffusion measurements: Spin echoes in the presence of a time-dependent field gradient. *J Chem Phys*. 1965;42:288–292.

34. Jones DK. *Diffusion MRI: Theory, Methods, and Applications*. New York: Oxford University Press; 2011.

35. Leemans A, Jeurissen B, Sijbers J, Jones DK. ExploreDTI: a graphical toolbox for processing, analyzing, and visualizing diffusion MR data. In: *Proceedings of the International Society for Magnetic Resonance in Medicine*. 2009.3537.

36. Basser PJ, Jones DK. Diffusion-tensor MRI: theory, experimental design and data analysis - a technical review. *NMR Biomed*. 2002;15:456–467. doi: 10.1002/nbm.783

37. Bankhead P, Loughrey MB, Fernández JA, Dombrowski Y, McArt DG, Dunne PD, McQuaid S, Gray RT, Murray LJ, Coleman HG. et al. QuPath: open source software for digital pathology image analysis. *Sci Rep*. 2017;7:1–7. doi: 10.1038/s41598-017-17204-5

38. Ruifrok AC, Johnston DA. Quantification of histochemical staining by color deconvolution. *Anal Quant Cytol Histol*. 2001;23:291–299.

39. Farrell JAD, Landman BA, Jones CK, Smith A, Prince JL, Zijl PV, Mori S. Effects of SNR on the accuracy and reproducibility of DTI-derived fractional anisotropy, mean diffusivity, and principal eigenvector measurements at 1.5T. *J Magn Reson*. 2010;26:756–767. doi: 10.1002/jmri.21053

40. Beare R, Lowekamp B, Yaniv Z. Image segmentation, registration and characterization in R with simpleITK. *J. Stat. Softw* 2018;86:1–35. doi: 10.18637/jss.v086.i08

41. Klein S, Staring M, Murphy K, Viergever MA, Pluim J. <emphasis emphasistype="mono">elastix</emphasis>: a toolbox for intensity-based medical image registration. *IEEE Trans. Med. Imaging*. 2010;29:196–205.

42. Shamonin DP, Bron EE, Lelieveldt BPF, Smits M, Klein S, Staring M. Fast parallel image registration on CPU and GPU for diagnostic classification of Alzheimer's disease. *Front. Neuroinform* 2014;7:1–15. doi: 10.3389/fninf.2013.00050

43. Shi C, Wei B, Wei S, Wang W, Liu H, Liu J. A quantitative discriminant method of elbow point for the optimal number of clusters in clustering algorithm. *Eurasip J Wirel Commun Netw*. 2021;31:1–16. doi: 10.1186/s13638-021-01910-w

44. Ratner B. The correlation coefficient: Its values range between 1/1, or do they. *J Targeting Meas Anal Mark*. 2009;17:139–142. doi: 10.1057/jt.2009.5

45. Ghazanfari S, Driessen-Mol A, Strijkers GJ, Kanters FMW, Baaijens FPT, Bouten CVC. A comparative analysis of the collagen architecture in the carotid artery: Second harmonic generation versus diffusion tensor imaging. *Biochem Biophys Res Commun*. 2012;426:54–58. doi: 10.1016/j.bbrc.2012.08.031

46. Flamini V, Kerskens C, Simms C, Lally C. Fibre orientation of fresh and frozen porcine aorta determined non-invasively using diffusion tensor imaging. *Med Eng Phys*. 2013;35:765–776. doi: 10.1016/j.medengphy.2012.08.008

47. Lally C, Flamini V, Kerskens C, Moerman KM, Simms CK. Imaging arterial fibres using diffusion tensor imaging-feasibility study and preliminary results. *EURASIP J Adv. Signal Process*. 2010;2010:6–8.

48. Carallo C, Tripolino C, de Franceschi MS, Irace C, Xu XY, Gnasso A. Carotid endothelial shear stress reduction with aging is associated with plaque development in twelve years. *Atherosclerosis*. 2016;251:63–69. doi: 10.1016/j.atherosclerosis.2016.05.048

49. Jani B, Rajkumar C. Ageing and vascular ageing. *Postgrad Med J*. 2006;82:357–362. doi: 10.1136/pgmj.2005.036053

50. Sertedaki E, Veroutis D, Zagouri F, Galyfos G, Filis K, Papalambros A, Aggeli K, Tsioli P, Charalambous G, Zografos G. et al. Carotid disease and ageing: a literature review on the pathogenesis of vascular senescence in older subjects. *Curr Gerontol Geriatr Res*. 2020;2020:8601762. doi: 10.1155/2020/8601762

51. Gijsen FJH, Vis B, Barrett HE, Zadpoor AA, Verhagen HJ, Bos D, Van Der Steen AFW, Akyildiz AC. Morphometric and mechanical analyses of calcifications and fibrous plaque tissue in carotid arteries for plaque rupture risk assessment. *IEEE Trans Biomed Eng*. 2021;68:1429–1438. doi: 10.1109/TBME.2020.3038038

BASIC SCIENCES - AL

52. Xie Y, Yu W, Fan Z, Nguyen C, Bi X, An J, Zhang T, Zhang Z, Li D. High resolution 3D diffusion cardiovascular magnetic resonance of carotid vessel wall to detect lipid core without contrast media. *J Cardiovasc Magn Reson.* 2014;16:1–10.

53. Kim S-E, Treiman GS, Roberts JA, Jeong E-K, Shi X, Hadley JR, Parker DL. In vivo and ex vivo measurements of the mean ADC values of lipid necrotic core and hemorrhage obtained from diffusion weighted imaging in human atherosclerotic plaques. *J Magn Reson Imaging.* 2011;34:1167–1175. doi: 10.1002/jmri.22736

54. Maurice P, Blaise S, Gayral S, Debelle L, Laffargue M, Hornebeck W, Duca L. Elastin fragmentation and atherosclerosis progression: the elasto-kine concept. *Trends Cardiovasc Med.* 2013;23:211–221. doi: 10.1016/j.tcm.2012.12.004

55. Urban Z, Peyrol S, Plauchu H, Zabot MT, Lebwohl M, Schilling K, Green M, Boyd CD, Csiszár K. Elastin gene deletions in Williams syndrome patients result in altered deposition of elastic fibers in skin and a subclinical dermal phenotype. *Pediatr Dermatol.* 2000;17:12–20. doi: 10.1046/j.1525-1470.2000.01703.x

56. Fornieri C, Quaglino D, Lungarella G, Cavarra E, Tiozzo R, Giro MG, Canciani M, Davidson JM, Ronchetti IP. Elastin production and degradation in cutis laxa acquisita. *J Invest Dermatol.* 1994;103:583–588. doi: 10.1111/1523-1747.ep12396893

57. Kuzan A, Chwiłkowska A, Pezowicz C, Witkiewicz W, Gamian A, Maksymowicz K, Kobielarz M. The content of collagen type II in human arteries is correlated with the stage of atherosclerosis and calcification foci. *Cardiovasc Pathol.* 2017;28:21–27. doi: 10.1016/j.carpath.2017.02.003

58. Stary HC, Chandler AB, Glagov S, Guyton JR, Insull W, Rosenfeld ME, Schaffer SA, Schwartz CJ, Wagner WD, Wissler RW. A definition of initial, fatty streak, and intermediate lesions of atherosclerosis. *Circulation.* 1994;89:2462–2478. doi: 10.1161/01.cir.89.5.2462

59. Homma S, Troxclair DA, Zieske AW, Malcom GT, Strong JP. Histological changes and risk factor associations in type 2 atherosclerotic lesions (fatty streaks) in young adults. *Atherosclerosis.* 2011;219:184–190. doi: 10.1016/j.atherosclerosis.2011.07.022

60. Young VE, Patterson AJ, Sadat U, Bowden DJ, Graves MJ, Tang TY, Priest AN, Skepper JN, Kirkpatrick PJ, Gillard JH. Diffusion-weighted magnetic resonance imaging for the detection of lipid-rich necrotic core in carotid atheroma in vivo. *Neuroradiology.* 2010;52:929–936. doi: 10.1007/s00234-010-0680-y

61. Jones DK, Horsfield MA, Simmons A. Optimal strategies for measuring diffusion in anisotropic systems by magnetic resonance imaging. *Magn Reson Med.* 1999;42:515–525. doi: 10.1002/(SICI)1522-2594 (199909)42:3<515::AID-MRM14>3.0.CO;2-Q

62. Peng S, Guo W, Morrisett JD, Johnstone MT, Hamilton JA. Quantification of cholesteryl esters in human and rabbit atherosclerotic plaques by magic-angle spinning 13C-NMR. *Arterioscler Thromb Vasc Biol.* 2000;20:2682–2688. doi: 10.1161/01.atv.20.12.2682

63. Lundberg B. Chemical composition and physical state of lipid deposits in atherosclerosis. *Atherosclerosis.* 1985;56:93–110. doi: 10.1016/0021-9150(85)90087-5

64. Choe AS, Gao Y, Li X, Compton KB, Stepniewska I, Anderson AW. Accuracy of image registration between MRI and light microscopy in the ex vivo brain. *Magn Reson Imaging.* 2011;29:683–692. doi: 10.1016/j.mri.2011.02.022

65. Stary HC, Chandler AB, Dinsmore RE, Fuster V, Glagov S, Insull W, Rosenfeld ME, Schwartz CJ, Wagner WD, Wissler RW. A definition of advanced types of atherosclerotic lesions and a histological classification of atherosclerosis. *Circulation.* 1995;92:1355–1374. doi: 10.1161/01.cir.92.5.1355